JOURNAL OF GEOPHYSICAL RESEARCH, VOL. 100, NO. C5, PAGES 8661–8675, MAY 15, 1995

A comparative study of tropical Pacific sea surface height variability: Tide gauges versus the National Meteorological Center data-assimilating ocean general circulation model, 1982-1992

David B. Enfield and Jesse E. Harris
Atlantic Oceanographic and Meteorological Laboratory, NOAA, Miami, Forida

Abstract. To help assess the effectiveness of the model-based analysis and prediction procedures at the National Meteorological Center (NMC), we compare the seasonal and nonseasonal components of sea level from 44 tide gauges in the tropical Pacific with those of the dynamic heights output by two 11-year model reanalyses (1982-1992) at the same locations, which differ mainly in their wind forcing. Both reanalyses assimilate ocean thermal data and incorporate most of the procedures used by NMC in producing operational ocean analyses and experimental coupled model climate forecasts. The reanalyses reproduce the broad patterns of annual amplitude and phase and of seasonal and nonseasonal variance, except for severe underestimates along the eastern boundary, especially north of the equator. The annual cycles and interannual departures of zonal flow indices estimated from selected island pairs near the dateline show good correspondence for the North Equatorial Countercurrent (NECC) and somewhat flawed and noisy comparisons for the North Equatorial Current (NEC) and South Equatorial Current (SEC). The reanalyses also reproduce the large-scale time and space patterns of nonseasonal variability in the first three empirical orthogonal functions (EOFs), which together explain about 65% of the anomalous variability and characterize the El Niño-Southern Oscillation cycle. The first two EOF modes describe the westward migration of three ENSO episodes, and the third mode appears to capture differences between episodes. However, the reanalysis based on the anomalous winds generated by the NMC medium-range forecast model shows significant discrepancies in the large-scale spatial and temporal variability. These discrepancies disappear in the reanalysis based on departures of the Florida State University analyzed wind fields. Hence the wind forcing critically affects the reanalysis in spite of the assimilation of ocean thermal data. Future improvements in the atmospheric model to produce a more realistic evolution of the wind field can therefore lead to significantly better model integrations in the analysis and initialization mode (with data assimilation) as well as in the coupled model forecast mode.

1. Introduction

The current state of the art in short-term climate prediction consists of integrating coupled oceanic and atmospheric general circulation models forward from an initial state, determined as much as possible through analysis of the most recent data fields, into future time. In any coupled model scheme an ocean general circulation model (OGCM) plays a key role by specifying the surface boundary temperature for the atmosphere. OGCM performance is extremely sensitive to the initial, three-dimensional ocean state, which may be in error due to insufficient assimilated data, nonoptimal assimilation methods, inaccurate wind forcing, or inadequate formulation of internal model dynamics. Faulty dynamical formulations, in particular, further exacerbate performance in the forecast mode (future time) where data are not available for assimilation and the model state may drift due to dynamical biases. Moreover, shortcomings in the atmospheric model to which the OGCM is coupled can generate inaccurate wind fields in response to surface forcing from the OGCM, thus causing erroneous results in successive time steps of the ocean model. By running OGCMs in an historical context with assimilated ocean data and specified wind forcing, reanalyses of ocean fields can be generated and assessed against independent data sets. The purpose of this paper is to perform one such assessment using sea surface height (SSH) as the comparison variable for historical reanalyses with thermal data assimilation produced by the U.S. National Oceanic and Atmospheric Administration (NOAA).

In the United States the responsibility for implementing advanced climate analyses and forecasts falls upon the NOAA National Meteorological Center (NMC). As part of a coupled-model climate forecast system now under development, NMC use a modified Bryan-Cox OGCM to produce operational weekly analyses or "nowcasts" of the tropical Pacific Ocean state. In the analysis mode the ocean model is constrained through the assimilation of sea surface temperature (SST) and three-dimensional thermal observations (expendable bathythermographs (XBTs) and moored buoys) and is forced by operational wind analyses from the NMC medium-range forecast model. The NMC Climate Analysis Center uses these nowcast fields of SST and dynamic variables such as velocities

Paper number 95JC00752.

and 20°C isotherm depths as elements for the production of the monthly Climate Diagnostics Bulletin. In addition, NMC is also experimenting with a multiseason, coupled-model climate forecast scheme, which allows the ocean model to interact with the atmospheric model after initialization by the most recent nowcast [*Ji et al.*, 1994].

NMC has used a variation of its operational assimilation scheme to reanalyze the monthly historical ocean fields (temperature, north and south velocity components, and salinity) for the 1982-1993 period [*Ji et al.*, 1995]. The reanalyses are designed to replicate the operational nowcast procedure in a uniform manner over past time, thus providing the required ocean initial conditions for simulated coupled-model forecast experiments. They are also a means by which NMC can involve the outside research community in the further development and evaluation of the analysis and prediction system. That is the role of the reanalyses in this study. Although the NMC reanalyses are produced somewhat differently than their nowcasting counterparts, the differences are minimal. Hence evaluations of the reanalyses can potentially provide useful guidance for improving the operational methods. Moreover, research oceanographers can use well-verified reanalyses as high resolution, dynamic interpolations of the sparser observed fields.

In this paper we take a first step toward evaluating the NMC ocean analysis system through a systematic evaluation of its effectiveness in reproducing past SSH variability in the tropical Pacific. The comparison data set consists of monthly time series of sea level from tide gauges at 44 Pacific locations between 40°S and 40°N. We perform bivariate comparisons (at each location) and multivariate comparisons (pattern fidelity) on two timescales: seasonal and departures from seasonal.

The reanalyses we use here are the RA2, referred to and described by *Ji et al.* [1995], and the subsequent RA3, which differs primarily in the wind field specification. In sections 2 and 3 we will summarize the main aspects of the procedures used in producing both nowcasts and the renalyses. Subsequent sections will compare the RA2 reanalysis with SSH from the tide gauge array in respect to their geographic distributions of annual and interannual variance (section 4), the amplitude and phase of the annual harmonic (section 5), the correlation of interannual departures (section 6), the behavior of zonal circulation indices (section 7), and the fidelity of large-scale interannual variability as represented by EOF modal analyses (section 8). In section 9 we describe the RA3 reanalysis and summarize the ways in which its performance differs with that of RA2, in particular, regarding the effects of the different wind forcing on large-scale interannual variability.

2. The Nowcasts and Reanalyses

The nowcasts and reanalyses are based on the assimilation of thermal profile data into the OGCM, with forcing provided by a hybrid model-data wind field history. We will only summarize the more salient features of the procedures, leaving the reader to consult descriptions such as *Derber and Rosati* [1989] and *Ji et al.* [1995] for greater detail. Of particular interest in this summary are (1) the way in which the ocean model is driven to produce the first-guess fields for each assimilation time step, (2) the procedures for the assimilation of SST and $T(z)$ data, and (3) the differences between the renalyses and the operationally produced nowcasts.

The ocean model used by NMC is an operational modification of the tropical ocean general circulation model developed at the NOAA Geophysical Fluid Dynamics Laboratory by *Bryan* [1969] and *Cox* [1984] and used in various well-known circulation studies [e.g., *Philander and Pacanowski*, 1981; *Philander et al.*, 1987]. The NMC model domain extends zonally across the entire Pacific and from 45°S to 55°N. Grid points are spaced at 1.5° intervals in longitude. Latitudinally, the spacing is 1/3° from the equator to 10° latitude, increasing to 1° at 20° latitude and constant at 1 degree, poleward of 20°. To suppress spurious numerical effects at the open boundaries, the 35-45°S and 45-55°N zonal bands are coded as 10° "sponge" regions in which the calculations are relaxed poleward toward climatology. The model bottom topography is variable, and there are 28 computational surfaces in the vertical. The layer interface depths are constant, and the layers are thinner and more tightly packed in the upper ocean.

The model forward steps calculations of the three-dimensional fields of temperature, salinity, and velocity in hourly time increments. Salinity is initially specified by the *Levitus* [1982] climatology and is modified thereafter by model fluxes with no sources or sinks (net freshwater influx at the surface is zero). Once a year, the salinity climatology is respecified. The temperature field is carried forward in a similar fashion but is constrained at every time step by the data assimilation procedure (described below). The geostrophic part of the model circulation comes from vertical integration of the resulting density fields.

The RA2 reanalysis procedure [*Ji et al.*, 1995] involves forcing the ocean model with 11-year monthly wind stress fields (July 1982 through June 1993) obtained by adding a model-simulated wind stress anomaly field to a data-based wind stress climatology. The climatology is that of *Harrison* [1989], with the stresses increased by 10%. The wind stress anomaly fields were obtained by forcing a reduced-resolution version of the NMC medium-range forecast (MRF) model with an analyzed SST history [*Reynolds*, 1988] and removing the simulated wind stress climatology.

In the RA3 reanalysis the hybridization of the wind field is similar, in that a data-based climatology is combined with an anomalous component from a different source. The wind field used was different in two important respects. First, the climatology used in RA3 was that of *Hellerman and Rosenstein* [1983], with the stresses decreased by 10%. Second, the anomalous component consists of departures of the Florida State Universtiy (FSU) hand-analyzed pseudo-stresses from their own climatology, with the application of a drag coefficient of 1.3. All reference to reanalysis in sections 4-8 implies only the RA2 reanalysis. Sections 9-11 will refer to both, specifically.

To produce a nowcast or a reanalysis, the SST and $T(z)$ data are continuously assimilated into the analysis scheme as "time" is marched forward in hourly increments. However, if only the data measured during the "current" hourly time step were assimilated, there would be very little information to constrain the model integration and the result would be noisy in both space and time. The assimilation procedure therefore creates a "sliding data window" of 2 weeks for SST (from 1 week before to 1 week after the time step) and 4 weeks for thermal profiles (2 before to 2 after). At each time step the data from the earliest hour of the previous data window are

discarded and a new hour of data is added at the end of the window. A temporal weighting factor is assigned to the data in decreasing proportion to the time separation from the current time step, and the weighted time average of the data in the window is computed within 4°x4° spatial bins (many of which may be empty). Finally, a variational technique [*Derber and Rosati*, 1989] is used to construct a three-dimensional correction function between the modeled thermal field (integrated forward from the last assimilation step) and the weighted time average of the data. The correction field relaxes smoothly to zero in data sparse regions, where the model field remains relatively unchanged. This assimilation procedure has the double effect of applying a low-pass time-space filter on the data and the resulting model-data analysis, while increasing the amount of data available at each step.

There are several ways in which the reanalyses differ from the operational nowcasts. The reanalyses are monthly averages of the hourly fields described above, while the nowcasts are weekly. However, the areas in which the reanalyses differ most are in the wind forcing and the assimilation of SST data. The subsurface temperature data (XBTs, moored buoys) are essentially unchanged between the nowcast and hindcast systems. In the real-time analyses (nowcasts) the available SST information from XBTs, ships, and satellite infrared sensors is blended in much the same way as is done separately to produce SST analyses [*Reynolds and Smith*, 1994]. In the reanalyses the actual historical gridded SST analyses are used instead. The net difference between the two approaches is minimal because the data and editing methods are very similar [*Ji et al.*, 1995]. Unlike the reanalyses, the wind fields used for nowcasts are entirely produced by the NMC atmospheric forecast model. This appears to be the greatest potential source of differences between the real-time and retrospective products (D. Behringer, personal communication, 1994).

3. Data and Analysis Methods

The period for our comparisons extends from July 1982 through December 1992; although the reanalyses extend into 1993, we could not complete the comparison data set from tide gauges beyond 1992. We obtained monthly averaged sea levels at 44 tide gauge locations in the tropical Pacific between 40°S and 40°N (Table 1 and Figure 1). We obtained most of the data (for all islands and several coastal stations) from the Pacific Sea Level Data Center at the University of Hawaii. We also archived and processed much of the data from Central and South America at the Atlantic Oceanographic and Meteorological Laboratory (AOML). We obtained some data from some stations in Mexico and California as monthly averages from the Permanent Service for Mean Sea Level.

We adjusted the SSH data from the tide gauges to account for the inverse barometer effect, whereby each millibar of increased surface atmospheric pressure depresses sea level by about 1 cm (static response). Hence the true subsurface pressure gradients in the ocean are the sum of the gradients associated with sea surface slopes and the gradients of atmospheric pressure. We obtained monthly averaged sea level pressure time series from the grid points of the NMC operational surface pressure analyses nearest to the tide gauges, then we added them (minus 1000 mbar) to the corresponding sea level time series (centimeters) at the tide gauges.

We derived SSH from the reanalyses by integrating the density field from the ocean bottom to the surface at the model grid point nearest each tide station (dynamic height). The average distance from a tide station to the reanalysis grid point is about 50 km (0.5 degrees of latitude); only three stations were farther than 100 km (see Table 1).

The reanalyzed SSH series cover the 126-month analysis period without gaps. Missing data from the tide stations are in the ranges of 1-10%, 11-20%, and 21-31% for 37, 5, and 1 stations, respectively (Table 1). To avoid the possibility that the comparisons could be biased by different amounts of data, we tagged the missing months at each tide gauge location and ignored them in the harmonic fits and other univariate calculations for the tide gauges as well as the corresponding reanalysis grid points.

All long-term means are removed from the data; the period-mean fields cannot be compared because the tide gauge datums cannot be related to each other. Although we begin the comparisons of variability by examining the gross statistics, all the later analyses involve either the annual or interannual (departure from annual) portion of the variability. We look at annual variability as either the sum of the annual (12-month) and next two higher (6- and 4-month) harmonics or as the annual harmonic alone. For any given time series the summed harmonics reproduce very faithfully the climatology that results from averaging all the data for each calendar month. The annual harmonic further provides a convenient way to

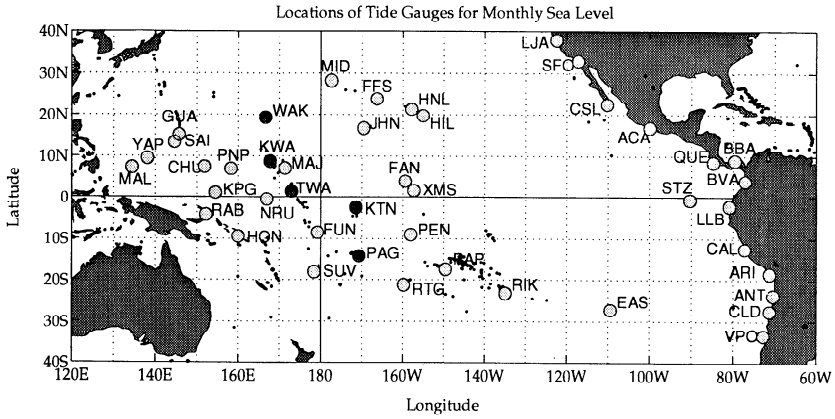

Figure 1. Area map for the tropical Pacific showing the locations of tide stations (round circles). The five darker circles are the locations used to calculate the zonal circulation indices shown in Figures 6 and 7. See Table 1 for station abbreviations.

Table 1. Nomenclature and Positional Information for Tropical Pacific Tide Gauges (TGs), Plus Standard Deviations of Tide Gauge Sea Level and Dynamic Heights From the Nearest Grid Points of the Model-Based RA2 Reanalysis (July 1982 - December 1992)

Station									
Number	Full Name	Abbre-viation	Latitude, deg	Longitude, deg	δpos, km	Percent of missing TG Data	σ(TGs), cm^2	σ(NMC), cm^2	$\Delta\sigma^2$, cm^2
10	Rabaul	RAB	-4.20	152.18	53		8.84	13.63	-107.7
1	Pohnpei	PNP	6.98	158.25	38		9.24	11.79	-53.5
57	Honolulu	HNL	21.30	202.13	37	9	4.34	6.82	-27.6
15	Papeete	PAP	-17.53	210.43	61	3	6.13	7.92	-25.2
16	Rikitea	RIK	-23.13	225.05	30		6.10	7.72	-22.4
52	Johnston	JHN	16.75	190.48	67	9	8.63	9.61	-17.9
60	Hilo	HIL	19.73	204.93	23	9	7.46	8.22	-12.0
55	Kwajalein	KWA	8.73	167.73	34	9	8.49	8.94	-7.8
13	Kanton	KTN	-2.49	188.57	60		7.76	8.19	-6.9
24	Penrhyn	PEN	-9.02	201.93	60	3	6.27	6.57	-3.8
54	Chuuk	CHU	7.45	151.85	35	12	7.50	7.45	0.8
7	Malakal	MAL	7.33	134.47	67		8.29	8.20	1.4
2	Tarawa	TWA	1.37	172.93	36		8.77	8.68	1.6
5	Majuro	MAJ	7.10	171.37	82		8.09	7.77	5.0
53	Guam	GUA	13.43	144.65	86	9	6.27	5.56	8.4
25	Funafuti	FUN	-8.53	179.22	79		10.62	10.13	10.3
88	Caldera	CLD	-27.50	288.75	33		12.04	11.51	12.6
81	Valparaiso	VPO	-33.50	287.25	56		7.99	7.05	14.0
50	Midway	MID	28.22	182.63	4	9	8.61	7.72	14.4
56	Pago Pago	PAG	-14.28	189.32	54	9	7.66	6.60	15.1
29	Kapingamaran	KPG	1.06	154.47	99	4	8.78	7.87	15.2
14	French Frigate Shoals	FFS	23.87	193.72	54	2	11.24	10.45	17.1
4	Nauru	NRU	-0.53	166.91	0	8	6.39	4.77	18.1
28	Saipan	SAI	15.23	145.75	48	2	10.34	9.40	18.4
91	La Libertad	LLB	-2.20	279.08	71		6.18	4.42	18.8
93	Callao	CAL	-12.61	282.75	77		7.81	6.50	18.8
30	Santa Cruz	STZ	-0.75	269.67	39		6.56	4.79	20.0
23	Rarotonga	RTG	-21.20	200.23	44		6.46	4.41	22.4
83	Arica	ARI	-18.57	288.75	58	2	10.57	9.25	26.2
80	Antofagasta	ANT	-23.65	289.60	49		10.12	8.72	26.4
11	Christmas	XMS	1.59	202.71	45		13.82	12.76	28.3
18	Suva	SUV	-18.13	178.43	29	14	11.64	10.32	29.0
9	Honiara	HON	-9.43	159.95	88		8.13	6.03	29.7
8	Yap	YAP	9.52	138.13	0	9	13.48	12.25	31.7
12	Fanning	FAN	3.90	200.62	0	31	10.40	8.74	31.7
87	Quepos	QUE	8.50	275.25	188		8.41	6.01	34.6
22	Easter Is	EAS	-27.15	250.55	0	6	6.93	3.62	34.9
51	Wake	WAK	19.28	166.62	0	9	7.45	4.44	35.8
551	SanFrancisco	SFO	37.80	237.53	97	18	8.61	5.71	41.5
554	La Jolla	LJA	32.87	242.75	0	18	9.91	7.22	46.1
316	Acapulco	ACA	16.83	260.08	186	23	10.54	7.72	51.5
85	Buenaventura	BVA	3.90	282.90	19	6	10.22	6.70	59.5
302	Balboa	BBA	8.97	280.43	62	3	11.81	7.27	86.6
34	Cabo San Lucas	CSL	22.50	249.75	117	16	13.04	6.41	128.9

Station numbers are by university of hawaii. Here dpos is the grid point offset; s(TGs) and s(NMC) are standard deviations for tide gauges and National Meteorological Center, respectively; and Ds2 is the difference in total variance (tide gauges minus RA2). Stations are sorted in order of increasing variance difference.

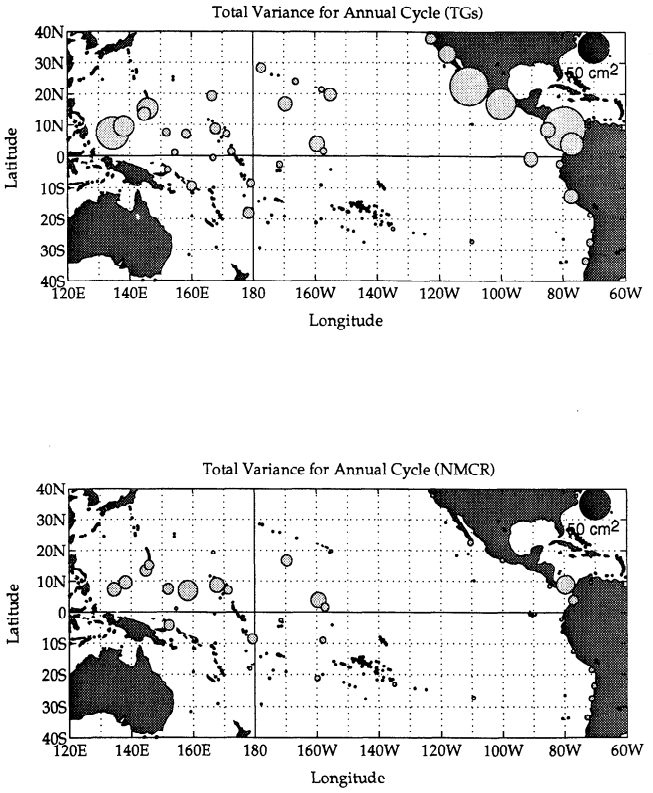

Figure 2. Distribution of variance for the annual cycle (summed harmonics) of sea surface height (SSH) (top) at 44 tide gauge locations and (bottom) the nearest National Meoeorological Center (NMC) reanalysis (RA2) grid points. Magnitudes are shown relative to a 50 cm^2 reference circle (darker circle, top right).

present and compare amplitude and phase information for the annual timescale. We use the departure time series, formed by subtracting the summed harmonics from the data, to analyze the interannual timescale, which is dominated by the three El Niño-Southern Oscillation (ENSO) cycles whosc warm phases occurred in 1982-1983, 1986-1987 and 1991-1992. We examine the annual and interannual timescales separately as to their distributions of variance and the way several island-based indices of zonal currents behave (a la *Wyrtki* [1974a,b]). The data sets are also compared as to their distributions of amplitude and phase of the 12-month harmonic. We compare the interannual variability by computing the zero-lagged cross-correlation between the two versions of SSH at each location. Finally, we subject both data sets to an empirical orthogonal function (EOF) analysis to compare the ways in which the departures separately reproduce large-scale temporal and geographic patterns of variability.

We calculate correlations and their significance in various places. Without exception we determine the significance levels by the method of *Sciremammano* [1979]. The method is equivalent to applying a standard t test using an adjusted ("effective") degrees of freedom, determined by accounting for the serial correlation (or the integral timescale) in the time series.

4. Variance Distributions

Table 1 shows the standard deviations for the tide gauges and the RA2 reanalysis. The distribution of variance differences (last column, tide gauges minus reanalysis) is bell-shaped with a mean of +15.2 cm^2 and a standard error of 5.4 cm^2. Thus the overall SSH variance from tide gauges is significantly greater than that of the reanalysis at the 99% significance level. Thirty-one locations show a variance difference farther from zero than the 99% significance level (±15 cm^2). Most of these are at the eastern boundary or at higher-latitude island stations (near ±20°), while most of the island locations between ±15° are within the 99% limits. There is no discernible geographical pattern of negative versus positive differences at island locations. However, all the eastern boundary locations (including the Galapagos) fall in the range of positive differences at or above the 98% significance level.

Variance circles plotted in Figures 2 and 3 illustrate the geographical variations of seasonal (summed harmonics) and nonseasonal variance, respectively. In the low-latitude interior the tide gauges and reanalysis have generally similar magnitudes, although differences are seen at individual stations. Both agree in showing that island stations have considerably greater variance in the nonseasonal component than in the seasonal band and that the seasonal variability is somewhat more energetic north of the equator.

Along the eastern boundary the two data sets tell very different stories. In the annual cycle (Figure 2) the tide gauge data contrast greatly across the equator. Along thc northern hemisphere coastline the annual variability for tide gauges is much larger than at island stations, while south of the equator, the opposite is true. The reanalysis shows a much smaller variation along the entire northern coastline and does not lead to the same conclusion (comparison to islands). The nonseasonal variability (Figurc 3) is also less energetic in the

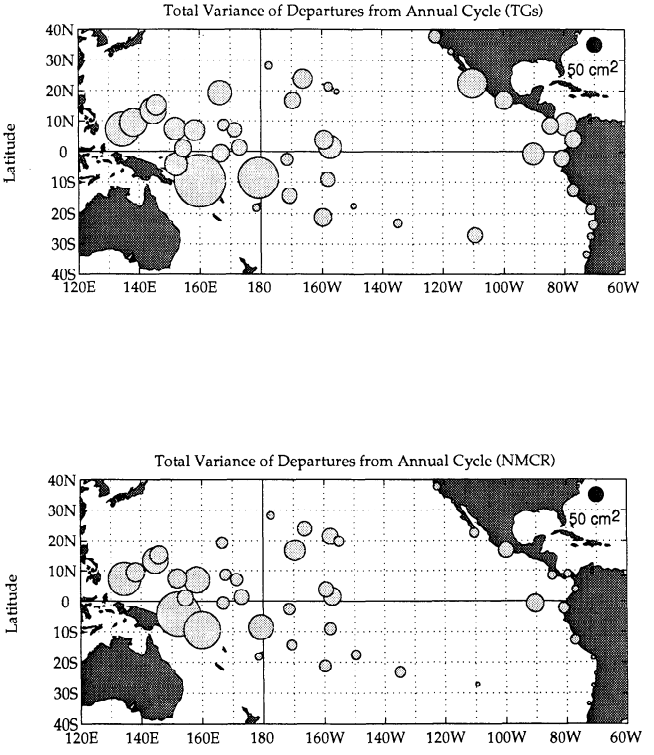

Figure 3. Same as Figure 2, but for the departures from the annual cycle of SSH.

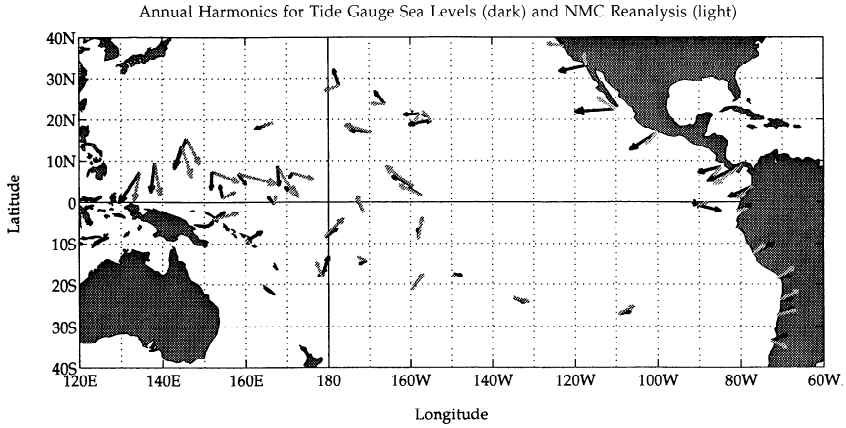

Figure 4. Distribution of the 12-month harmonic of SSH from tide gauges (solid arrows) and the NMC reanalysis (stippled arrows). Annual phase is oriented about a clockface, with January and December corresponding to 1 o'clock and 12 o'clock, respectively. When vectors are collinear, the light vector obscures the dark vector.

reanalysis than for tide gauges, especially north of the equator, although not as drastically. In summary, all indications are that the RA2 reanalysis variability is systematically too small along the eastern boundary, especially north of the equator, but generally reasonable elsewhere.

5. The 12-Month Harmonic

Figure 4 shows a vector "clock plot" of the amplitude and phase of the complex-valued annual (12-month) harmonics of SSH for the RA2 reanalysis and tide gauges. The vector amplitudes in Figure 4 tend to reflect the comparison of annual variance shown in Figure 2 (top), but differences are less enhanced (lack of squaring) and higher-frequency contributions (higher harmonics) are not included. The reanalysis amplitudes are generally similar to those of tide gauges in the ocean interior and along the South American coast, while they are smaller along the eastern boundary north of the equator (consistent with the variance analysis).

An objective measure of the correlation between two complex-valued variables is the inner cross-correlation R_i as defined by *Mooers* [1973]. R_i is the modulus of the complex-valued result of subjecting two complex variables to a standard cross-correlation computation as normally applied to real scalar variables. In the case of Figure 4, computation of the inner cross-correlation between the annual harmonics of the reanalysis and tide gauges yields $R_i = 0.74$ (pattern correlation over the location array). This merely reflects quantitatively what is qualitatively obvious by inspection of Figure 4, that the two sets of harmonics exhibit similar patterns.

In spite of the general agreement in patterns implied by the outer cross-correlation, there are systematic phase differences in certain regions. The annual phase for the reanalysis tends to lead the tide gauge data by 1-3 months in the central North Pacific, north of 20°N, and in the far western Pacific north of the equator. The reanalysis lags by about 2 months on the equator northeast of New Guinea and by 2-4 months at Cabo San Lucas and San Francisco.

6. Correlation of Departures

Figure 5 shows how each of the tide gauge departure series correlates with its RA2 reanalysis counterpart (nearest grid point). The magnitude of each circle is shown in proportion to the estimated 95% significance level in each case, which always corresponds to the reference circle shown in the top right corner. The average 95% reference correlation for locations in the array is 0.50 and does not vary widely, such that a correlation of 1.0 corresponds to a solid circle approximately twice the diameter of the reference circle. The largest correlations, in the range of 0.85-0.95, are at low latitudes along the eastern boundary and north or south of the equator, west of 140°W. Groupings of marginal correlations, near the reference value where the RA2 explains considerably less than half the variance in tide gauge SSH, occur near the equator and dateline and at locations 20° or more off the equator.

One might expect that the correlations would reflect the abundance of assimilated subsurface thermal data. However, the distributions of assimilated Tropical Atmosphere-Ocean (TAO) buoys and XBT observations do not explain the correlation pattern in any obvious way. In the most general way the correlation pattern is consistent with the excellent temporal sampling of $T(z)$ within 10° of the equator by the moored TAO arrays. However, the TAO moorings were not numerous until near the end of the analysis period, and many of the better correlations are found poleward or east of the buoy positions. XBT observations available for assimilation become significantly less dense in the southeast Pacific off Peru and Chile, yet correlations there are high as far as the southern tropic. However, the coverage by XBTs over the interior north of 20°N is better than 20°S-20°N, which is inconsistent with the northward decrease in correlations. XBT observations are also plentiful along the eastern boundary north of the Gulf of Panama, again not explaining the poleward degradation in correlations there.

Other explanations seem more plausible. For example, the wind forcing along the eastern boundary and/or the OGCM response to it may be increasingly deficient in the poleward direction, while the influence of remote interior processes (through wave propagation) lessens poleward. The NMC medium-range forecast model, used to generate the anomalous component of the RA2 wind field, is optimized for the tropics and presumably deteriorates poleward. The MRF grid spacing does not resolve orography well along the west coast of the Americas, which is possibly more of a factor as the mountain

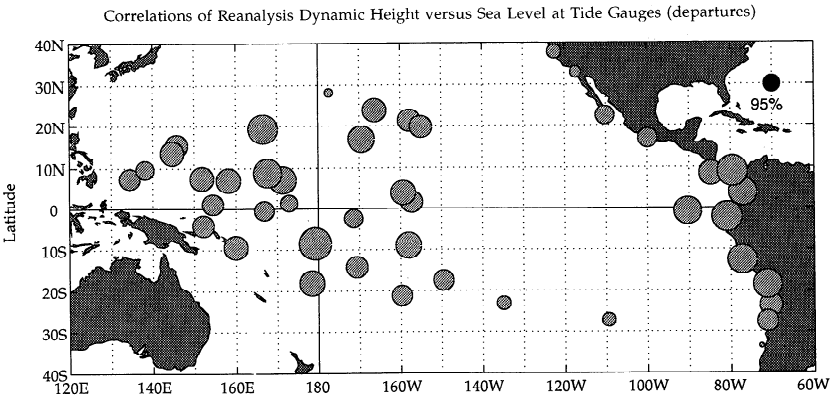

Figure 5. Relative magnitudes of the correlation coefficients of SSH departures for tide gauges versus their (RA2) reanalysis counterparts. The correlations are shown as stippled circles whose sizes are proportional to the 95% significance level at each location (invariant in size). The 95% significance level is shown as the reference (solid) circle in the top right corner of the map, and its numerical value is approximately 0.5 for these data sets.

ranges increase in altitude and breadth away from the equator. Moreover, the OGCM grid spacing (1.5 degrees in longitude) offers less resolution in the poleward direction, in relation to the coastal Rossby radius of deformation, so that the model becomes less able to emulate the dynamical processes that affect coastal sea level as a response to local wind forcing. All of these ideas are speculative. However, we will return to the issue of the anomalous wind field in section 9.

7. Zonal Circulation Indices

Using data from the 1950s and 1960s, *Wyrtki* [1974a,b] showed that differences between monthly averaged SSH at island stations straddling the equatorial currents can be used as diagnostic indices of the zonal flows, both seasonally and interannually. Here we compare the behaviors of similarly computed indices for selected tide stations and their nearest RA2 grid points to determine how well the known variabilities of the zonal flows are reproduced during our analysis period.

We have chosen five island stations for this analysis, shown by the darkly shaded symbols in Figure 1. With only one exception these are the same stations used by *Wyrtki* [1974a] to create indices of the North Equatorial Current (NEC, Wake minus Kwajalein), the North Equatorial Countercurrent (NECC, Tarawa minus Kwajalein), and the South Equatorial Current (SEC, Pago Pago minus Kanton). We substitute Tarawa for Christmas Island (Wyrtki's choice) in the NECC calculation, so that the NECC index does not span such a large range of longitudes (we now know that the near-equatorial SSH behaves much differently between the western and central Pacific). Figures 6 and 7 show the annual and interannual variabilities of the three zonal current indices, respectively. The series means have been subtracted, so that only the strengths relative to the annual means are shown. Positive (negative) values indicate stronger (weaker) flow in the direction of the mean current.

Both the annual and interannual behaviors of the tide gauge and RA2 indices are similar to those of *Wyrtki* [1974a, b] in two fundamental respects that should not depend on the different observation periods. First, the annual amplitudes and phases are similar, with the northern hemisphere (southern hemisphere) currents being strongest during the corresponding fall-winter period. Second, the interannual fluctuations also change phase across the equator, the NH (SH) indices being strongest during ENSO (non-ENSO) periods.

Differences also occur in the annual variability between the 1980s and Wytki's earlier period and between the tide gauges and the RA2 reanalysis. The tide gauge indices in Figure 6 are most similar to *Wyrtki*'s [1974a] for the NECC [*Wyrtki*, 1974a, Figure 7], with a maximum flow in December, weakest flow in April, and a "shoulder" of near-average flow during the northern hemisphere (NH) fall. The RA2 reproduces the peak and the trough but not the shoulder. The 1980s tide gauge index for the NEC indicates stronger than average flow from August through January, while *Wyrtki* [1974a] shows July through January and the reanalysis indicates September through February (1-month lag with respect to the contemporaneous tide gauges). The SEC flow was above average from April through August during the 1950s and 1960s [*Wyrtki*, 1974a, Figure 8] and from April through October for the 1980s tide gauges. The reanalysis shows above average SEC flow from June through October, weaker than for tide gauges during that period, but almost identical during the remainder of the year.

It is interesting that the interdecadal differences in the annual variability of tide gauge indices (*Wyrtki*, [1974a] versus Figure 6 of this paper) appear to be smallest for the NECC, which is the one index where we use a different island from Wyrtki's choice: Tarawa instead of Christmas. This suggests that these islands may differ markedly in their interannual behavior but not in their seasonal fluctuations. The interdecadal differences for the NEC and SEC are not large either and can be easily accounted for by their inclusion of different ensembles of interannual events in the averaging periods used. Again, it seems remarkable that the NECC appears to be the most stable of the three currents in the presence of strong interannual variability that is known to not adhere strongly to a canonical pattern of onset phase and propagation.

The departure time series (Figure 7) show interannual variability that is clearest for the NECC and best reproduced by the RA2 for that index (Figure 7, middle). The NECC series show large interannual swings, with strongest flows during early stages of the ENSO warm events of 1982-1983, 1986-

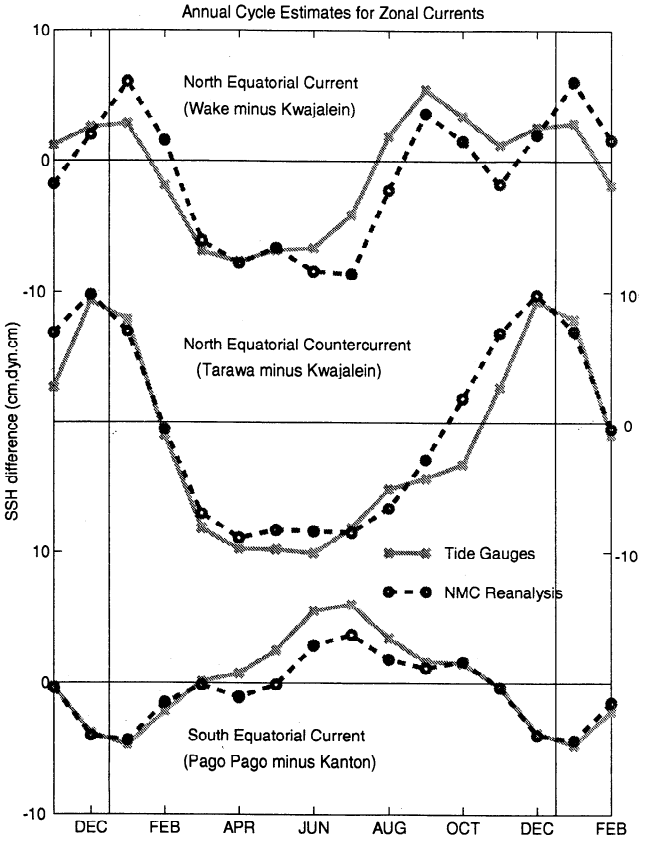

Figure 6. Annual cycles (three summed harmonics) for the zonal circulation indices of *Wyrtki* [1974a] computed from sea level differences between selected island locations (darker circles of Figure 1). The light, solid curves refer to the tide gauge data, and the dark, dashed curves to the corresponding grid points of the RA2 reanalysis. Series means are removed, and values are positive in the normally understood sense for each current (westward for the North Equatorial Countercurrent (NECC), eastward elsewhere).

1987 and 1991-1992 and weakest flow during the ENSO cold phases (1984-1985, 1988-1989). This behavior is also consistent with island data for the 1950s and 1960s [*Wyrtki*, 1974b]. However, the NECC index leads somewhat the phase of the ENSO cycle as it occurs in the central Pacific region of rapid unstable growth. The maximum flows, in particular, precede by as much as 6 months the known periods of prototypical warm anomalies in the central and eastern equatorial Pacific. This is because the equatorial western Pacific sea levels (e.g., at Tarawa) reach their peak values during the early stages of ENSO events (e.g., 1982) and are lowest during the later stages (e.g., the first half of 1983).

The tide gauge indices for the NEC and SEC show a more energetic mix of higher frequency (month-to-month) variability (Figure 7, top and bottom). The RA2 reanalysis replicates this whiter spectrum in both cases, as contrasted with the redder NECC. The RA2 docs not reproduce the NEC index as well as the NECC index, but the discrepancies occur more at the high frequencies than at the low frequencies. The reanalysis is least skillful at reproducing the SEC index, showing notable discrepancies throughout the spectrum.

8. Large-Scale Pattern Variability

The above comparisons involve pointwise pairings and as such include annual and subannual (intraseasonal, month to month) as well as interannual variability, and local as well as large-scale processes. The purpose of the NMC procedures is primarily to reproduce and predict the largest time and space scales, with an emphasis on residual variability (departures from an annual cycle). To be truly successful, then, the NMC procedures should at minimum perform well in reproducing temporal and spatial patterns of the residual variability at the largest scales: interannual and basin-wide. To test this we subjected the nonseasonal component of each data set (ensemble of stations) to a multivariate eigenvalue (EOF) decomposition. We deem the RA2 reanalysis successful insofar as it reproduces the hierarchically arranged eigenvectors and time coefficients of the tide gauge array.

Each EOF decomposition is based on 42 of the 44 tide gauge locations or the RA2 grid points nearest to those locations. We eliminated Fanning and Cabo San Lucas from the analysis because of excessive gappiness in the tide gauge data. Because only the largest timescales are in question, we filled a number of small gaps in the remaining tide gauge series using a two-sided autoregressive filter.

Figure 8 shows the sorted eigenvalues (percentage of total variance), their cumulative sums, and the zero lag correlations of time coefficients (between the tide gauges and the

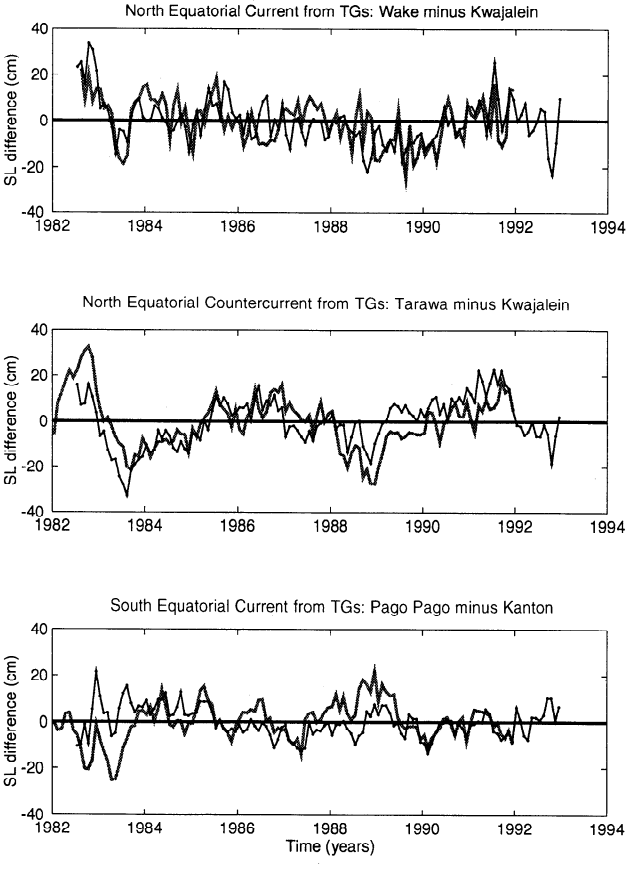

Figure 7. Departures from the annual cycles of the zonal circulation indices as calculated by *Wyrtki* [1974b] from sea level differences between selected island locations (dark circles of Figure 1) for the (top) NECC, (middle) North Equatorial Current (NEC), and (bottom) South Equatorial Current (SEC). The thick, stippled curves are for the tide gauge data, and the thin, solid curves are for the RA2 reanalysis.

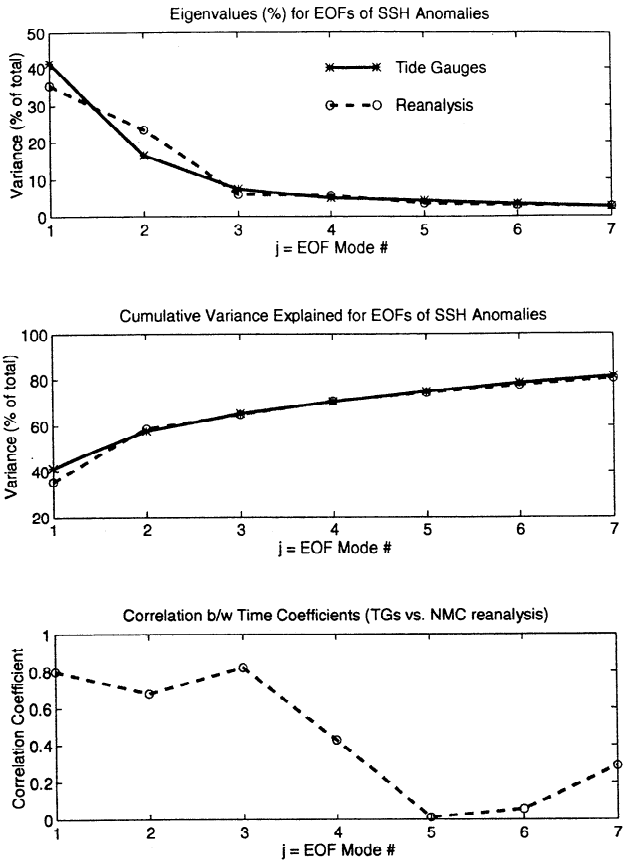

Figure 8. (top) Variance and (middle) cumulative variance explained by the first seven Empirical Orthogonal Function (EOF) modes of the tide gauge data and the RA2 reanalysis and (bottom) the correlations between the corresponding series of temporal expansion coefficients.

reanalysis). The first two modes in both data sets explain nearly 60% of the total variance. The explained variance drops off rapidly to the 5-8% range for the third and fourth modes. The first RA2 mode explains 7% less variance than its tide gauge counterpart, but this is compensated for in the second mode, making the cumulative increase almost identical for the second and higher modes.

The time coefficients of the two data sets correlate at 0.80, 0.68, 0.82, and 0.43 for the first four modes (Figure 8, bottom), then fall off to insignificant (<90%) values by mode 5. The number of correlations (mode 5 and higher) that reach significance is only that expected by chance, and the variance explained by them individually is very small. The small correlation value for higher modes reflects the tendency for the proportion of noise to increase with diminishing spatial scale and for whatever processes or local variabilities are common to the two data sets to fall out in different mode numbers. Whatever large-scale variability is reproduced by RA2 appears to be found in the first three or four modes.

The correlations for the time coefficients of the first three modes (Figure 9) are visually good. The high values in the first mode are clearly associated with the three ENSO warm phases because of their coincidence with the known ENSO history of the last two decades and because the eigenvectors load positively (negatively) in the eastern (western) Pacific, as seen in Figure 10. The series do not extend into the 1992 ENSO period due to incomplete tide gauge data, hence we only see the beginning of that event in 1991. The two first modes are similar, but there is a suggestion of a quadrature lag in the first mode with respect to the second, indicating propagation. This is confirmed by the lagged cross-correlations between the first two modes, which reach significant extreme values at lags of 12-18 months in the sense of eastward propagation (not shown). This is consistent with the observed event intervals of 4-5 years.

The largest discrepancy in the time coefficients (Figure 9) is what appears to be a lag of the RA2 reanalysis with respect to the tide gauges in the first two modes. Although small-scale perturbations are in phase, the low-frequency, interannual shifts appear lagged by several months during the first half of the record. However, the maximum lagged cross-correlation only improves to 0.82 at a 1-month lag.

Figure 10 shows the spatial distributions of the first three modes. These are hybrid representations in which the absolute value at each location is the percentage of variance explained by the mode at that particular location, i.e., the squared correlation coefficient (times 100) between the data at that location and the time coefficients for the mode. This gives information similar to that of the eigenvectors (loadings) but is more meaningful for how a mode's importance is distributed over the data array. The signs appropriate to the eigenvectors are also shown, so that in-phase and out-of-phase relationships can be easily distinguished in the same figure.

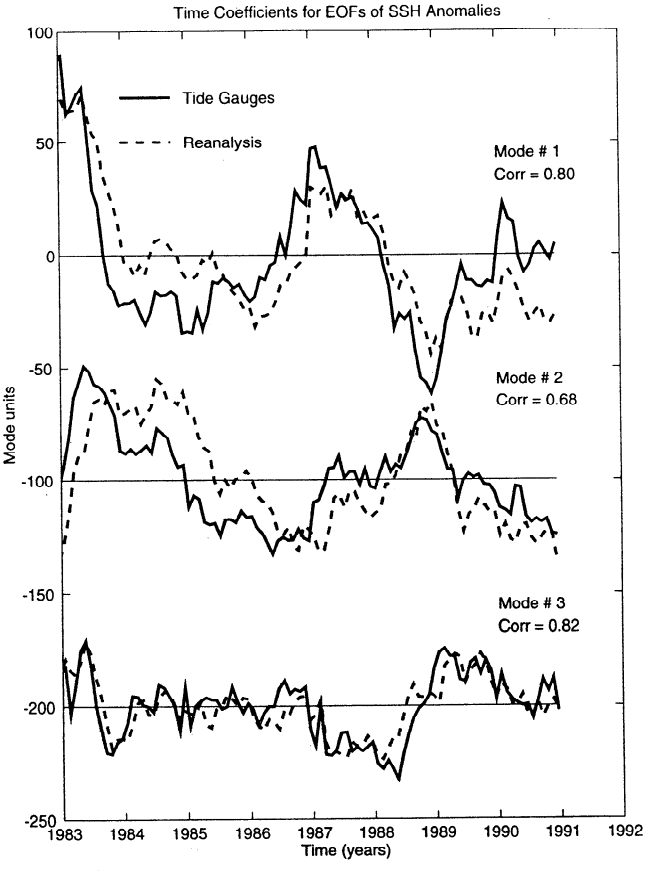

Figure 9. Temporal expansion coefficients for the first three EOF modes of sea surface height in the tide gauge data and the RA2 reanalysis, including the numerical values of the correlations shown in Figure 8 (bottom).

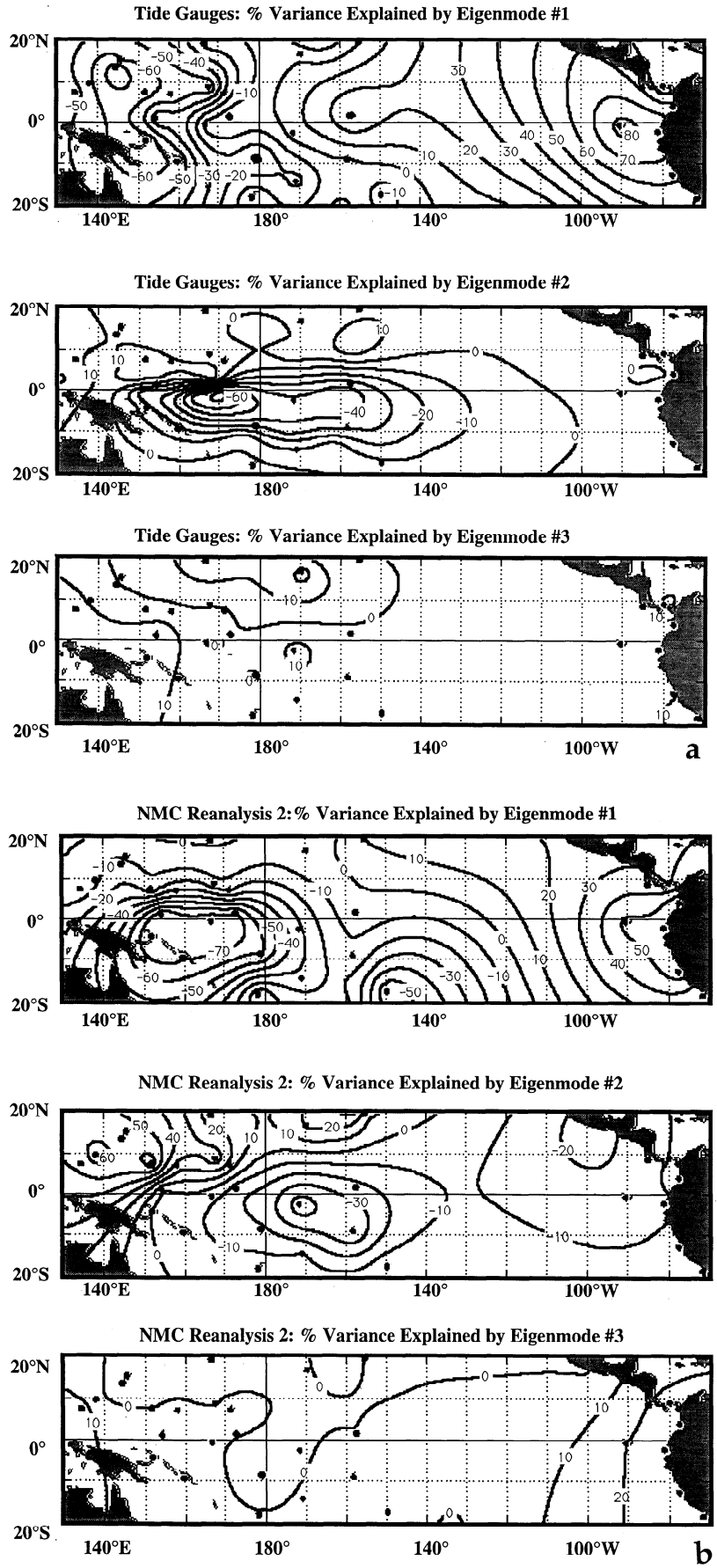

Figure 10. Spatial distributions of the signed variance explained for the first three EOF modes of departure variability in SSH, including (a) distributions for tide gauges and (b) distributions for the RA2 reanalysis.

We use a Kriging procedure to contour the information, but the contour details in the data-sparse region of the eastern Pacific are meaningless because the gaps are much larger than the decorrelation scales in the data.

The first mode of the tide gauge EOFs (Figure 10a, top) represents the ENSO-related seesaw between the eastern Pacific (positive, in phase with the time coefficients) and the far western Pacific (out of phase). The second mode (Figure 10a, middle) is in quadrature spatial phase to the first, being important in the dateline region between the antinodes of the first mode. Hence the first two modes, in both data sets, represent the propagating ENSO process with the propagation speed appropriate to an eastward migration of low-latitude heat content anomalies. In half of an ENSO cycle (2 to 2.5 years) a given phase (high or low sea level) propagates from New Guinea to the Galapagos. The process represented is the progression of thermal structure anomalies associated with ENSO (thermocline depth, heat content) rather than SST.

We note that the mode 1 and 2 ENSO patterns of the RA2 EOFs (Figure 10b, top and middle) are broadly similar to their tide gauge counterparts (Figure 10a), with the out-of-phase behavior between east and west (mode 1) and the quadrature component in the dateline region (mode 2). Together, these modes are also consistent with a slow eastward propagation of the anomalous thermal structure. However, both modes also show notable discrepancies. The most obvious differences are west of the dateline, especially in mode 1 and north of the equator. The second mode response is also badly mismatched west of the dateline, with greater positive (negative) loadings north (south) of the equator. The reanalysis also appears to have undue importance in the eastern Pacific off Central America. However, this is based only on the coastal gauges, where we already know from the pointwise comparisons that the variability is underestimated in the reanalyses. We have no indications of performance in the eastern Pacific interior region.

The third mode in the tide gauges (Figure 10a, bottom) seems to represent in-phase variability on the north side of the Interetropical Convergence Zone (ITCZ) in the central and west-central Pacific, which is out of phase with the region around New Guinea and northeastern Australia and to some extent with the region off Chile and Peru. Negative loadings are largest in a band centered along 15-20°N (Johnston, Wake, and Hawaii), while the largest positive values are around the Australia-New Guinea region and off subtropical South America. In the reanalysis the pattern of loadings is similar in the distribution of signs but with more emphasis on the region off South America and less in the region west of Hawaii. In both data sets the variability is predominantly interannual (Figure 9) but without a consistent phase relationship to the ENSO episodes detectable in the first two modes. We surmise that the third mode probably represents significant differences in how the tropical Pacific thermal structure evolved during these ENSO events. The reanalysis seems to capture much of this difference field and suggests that further analysis of the denser reanalysis grid could lead to insights about the processes involved.

The spatial distributions in the fourth mode bear little resemblance to each other (not shown). We conclude that the time correlation (0.43, Figure 8), though statistically significant, is probably spurious. Virtually all the large-scale information replicated in the RA2 reanalysis is found in the first three modes, which together explain about 65% of the

The large differences in the distributions of the mode 1 and 2 variability west of the dateline suggests that the OGCM's Rossby wave response to interannual wind forcing may be in error somehow. The most plausible explanation is through incorrect forcing by the anomalous component of the wind field. We consider this issue in the following section.

9. The Effects of Wind Forcing: The RA3 Reanalysis

In the latter stages of our study the NMC made another reanalysis available to us (RA3), whose principal difference lies in the wind field used to force the OGCM. As noted in section 2, RA3 uses the *Hellerman and Rosenstein* [1983] climatology reduced by 10%, instead of the *Harrison* [1989] climatology, increased by 10%. For the anomalous variability, RA3 uses the FSU pseudostress data instead of the departure fields generated by the NMC medium-range forecast model (MRF) in response to observed SSTs. RA3 was also run for a slightly different period: February 1982 through December 1993. We therefore repeated the analyses of Sections 4-8 with respect to comparisons between the tide gauge data set and RA3 but for the same period as for RA2. Here we briefly discuss the results corresponding to sections 4-7 and their relation to differences in climatological wind forcing. We then discuss in greater detail the results from our analysis of the large-scale interannual variability (EOFs, as in section 8), which show considerable improvement over RA2.

The RA3 comparisons corresponding to sections 4-7 show such insignificant differences with respect to the RA2 comparisons that the figures need not be shown. All the salient aspects already noted for RA2 also apply to RA3. In particular, we see the same similarities and discrepancies in the distributions of variance and annual variability and in the variability of zonal current indices. Interannual departure correlations are also very similar, except for a few isolated stations that do not alter the overall conclusions.

It should perhaps not surprise us that annual variability is similar in RA2 and RA3 because the wind climatologies are also similar. In his suggestions for improving the HR climatology, *Harrison* [1989] argued for using a similar compilation of wind observations but with a more modern version of the drag coefficient that varies with stability in the marine boundary layer. He noted that the two climatologies have broadly similar distributions and features but that the Harrison drag coefficients are about 20% smaller than for the HR climatology. In their wind field adjustments (+10% for RA2 and -10% for RA3), NMC effectively altered both climatologies toward the middle of the range observed by Harrison for the two approaches. Figure 11 (top and middle) shows the period mean stress distributions as altered by the NMC procedures and their difference field. The differences are clearly quite small in relation to the fields themselves, especially within ±10° of the equator and west of 140°W. The ratio of the rms spatial variation of the differences to that of the average of the two climatologies is 0.19. The principal difference between the distributions is that the RA3 stress magnitudes are somewhat stronger in the trade wind belts poleward of ±10°.

When we subject the RA3 departures of SSH to the EOF analysis, the first two modes have expansion (time) coefficients that are very similar to those of the tide gauges

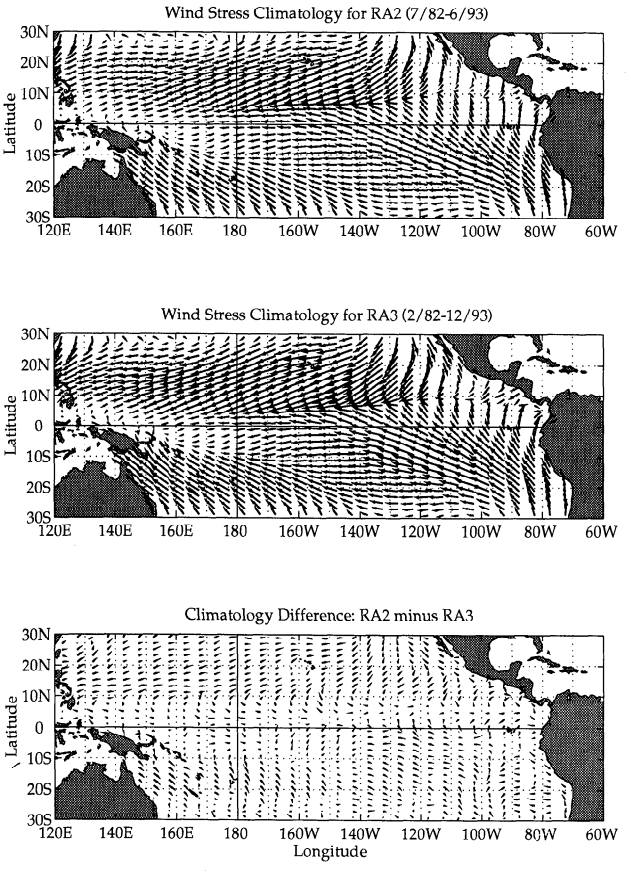

Figure 11. Climatological wind stress distributions for the (top) RA2 model run with the NMC medium-range forecast (MRF) model winds, (middle) RA3 model run with the Florida State University (FSU) analyzed winds, and (bottom) the distribution of the vector differences between the two climatologies.

(Figure 12) and RA2, and the variance breakdown by mode is also very similar (not shown). However, the unrealistic lag effect previously noted for RA2 (Figure 9) is now absent, and the cross-correlations between corresponding modes (1 and 2) are considerably higher. Another major difference is in the geographic distributions of explained variance for the first two modes (Figure 13). These are also more like the tide gauge distributions (Figure 10a) than are the RA2 patterns (Figure 10b). As with the tide gauges, the negative loadings in the first mode in RA3 are weaker, extend farther west of the date-line and farther north of the equator, while the positive loadings in the eastern Pacific explain more of the variance. The negative loadings of the second or quadrature mode (Figure 13, middle) are larger than for RA2 (Figure 10b, middle). Moreover, they are distributed along a longer zonal equatorial band between the Line Islands (150°-160°W) and New Guinea, also in better agreement with the tide gauges.

The third RA3 mode is qualitatively similar to the tide gauges in the tendency for negative (but weaker) loadings north of the equator in the central and west-central region and positive loadings around Australia-New Guinea and off South America. In its details, however, the third mode of RA3 appears to be somewhat more similar to RA2 than to the tide gauges.

To explore the differences in the wind field departures, we performed vector ($U + i*V$) EOF analyses on the RA2 and RA3 residual winds after averaging both fields onto an identical grid of 2°x 5° bins. We show the first-mode eigenvector distributions and their vector differences in Figure 14. The expansion (time) coefficients (not shown) are very similar to those of the SSH analyses (Figure 9) but opposite in sign. Hence the distributions of the RA2/MRF and RA3/FSU winds in Figure 14 (top and middle) correspond in sign to the cold phases of the ENSO cycles seen in Figures 9 and 12. The ratio of the rms spatial variation of the EOF differences to the averaged rms variations of the two EOF fields is 0.80. The relative importance of these differences is clearly much greater than for the climatologies (Figure 11).

Both RA2/MRF and RA3/FSU show a strengthening of equatorial easterlies along and just south of the equator during cold events. This is the feature principally associated with the ENSO cycle. Both fields show a westerly enhancement east of Australia in the South Pacific Convergence Zone and stronger flow away from the equator into the ITCZ (5°-10°N). The latter feature is consistent with a strengthening and northward migration of the ITCZ and a weakening of the low-latitude NE Trades east of the dateline. However, in RA3 the zone of equatorial easterlies extends farther eastward to 125°W and lacks the westerly anomalies (weaker trades) seen in RA2 farther east. The ITCZ variability is clearly much greater for RA2/MRF and penetrates farther eastward to Central America. Conversely, the RA2/MRF zone of westerly anomalies near 15°-30°S reaches only to 165°W, while the same feature in RA3/FSU reaches 110°W.

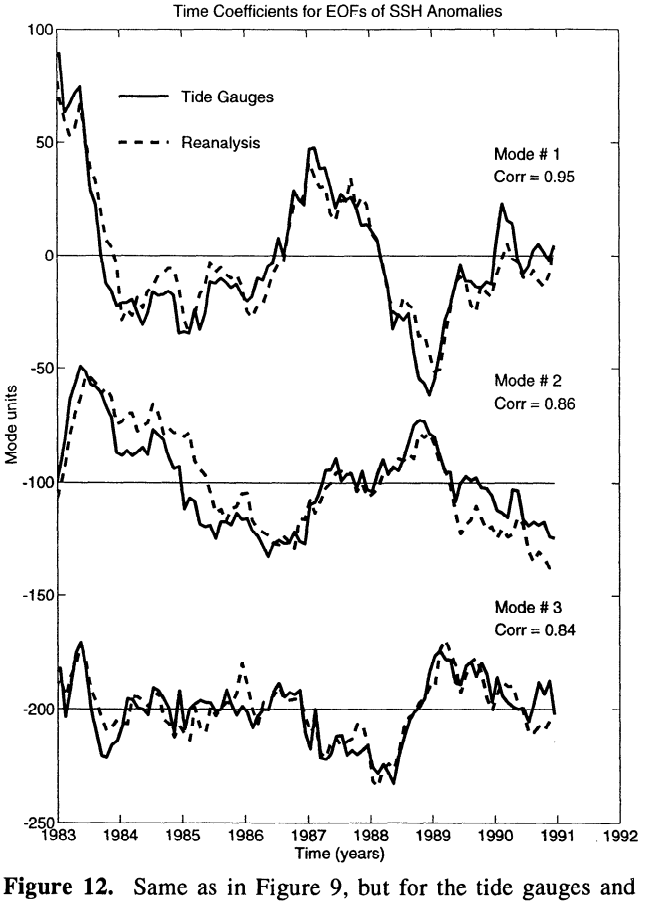

Figure 12. Same as in Figure 9, but for the tide gauges and RA3 reanalysis.

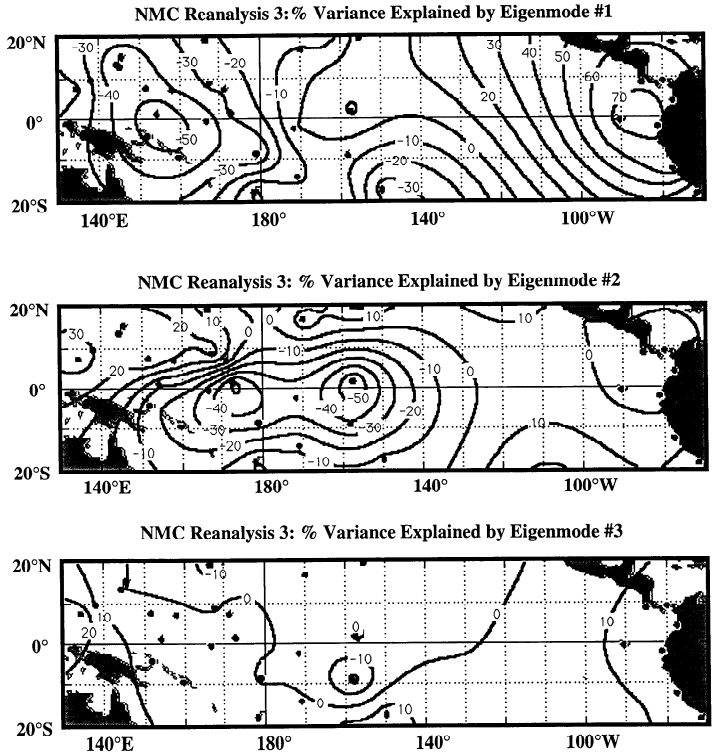

Figure 13. Same as in Figure 10b, but for the RA3 reanalysis.

Between 10°S and 10°N there is a broad pattern of eastward vectors in the RA2-RA3 difference field (Figure 14, bottom). In the region of strong ENSO forcing, near the equator and west of 120°W, these differences imply that the RA2/MRF winds show less strengthening (weakening) of easterly stress during ENSO cold (warm) phases than RA3/FSU. This discrepancy can be expected to alter the evolution of near-equatorial dynamic height, east of the dateline, primarily associated with ENSO through the zonal integral of the zonal wind stress. This is consistent with a weaker east Pacific amplitude in the first mode of RA2 dynamic height. Another factor is the effect of Rossby wave propagation to west of the wind anomaly region found straddling the equator near and to the east of the dateline. In RA2/MRF, the equatorial easterlies east of the dateline show less strengthening (weakening) during cold (warm) phases than RA3/FSU, consistent with a smaller (delayed) Rossby response to the west in mode 2.

Regional differences in wind stress curl may also be reflected in quasi-contemporaneous (same mode) features away from the equator. Thus, for example, the RA2/MRF winds are more easterly along 10°N and west of the dateline (Figure 14, bottom) associated with greater cyclonic and anticyclonic curl south and north of that latitude. This is consistent, respectively, with greater and lesser thermocline depression (and dynamic height) as seen in the first-mode distributions of Figure 10 (top) and a more realistic western Pacific pattern for RA3 (Figure 13, top).

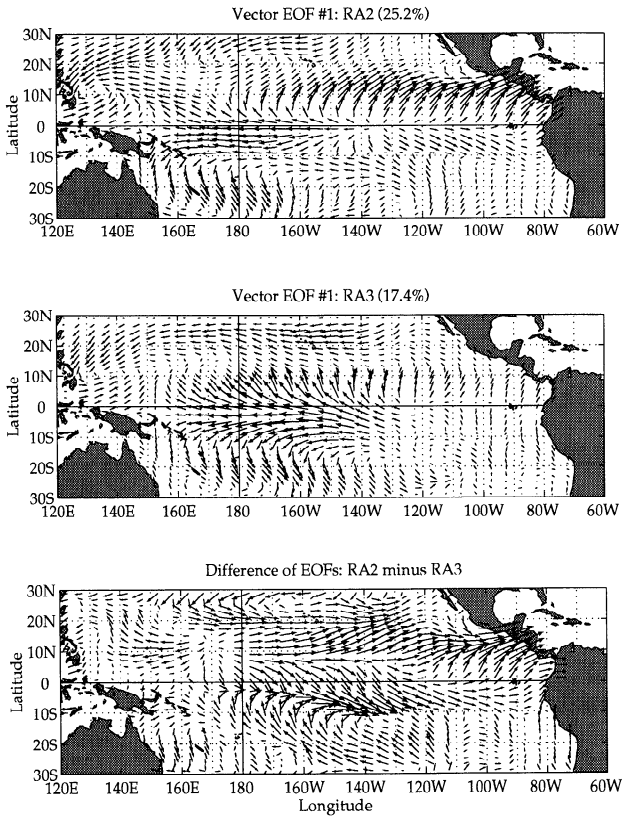

Figure 14. Spatial distributions of the first EOF mode eigenvectors of the (top) RA2/MRF and (middle) RA3/FSU winds. The directional sense corresponds to wind conditions during the cold phases of El Niño-Southern Oscillation cycles. (bottom) The distribution of the vector differences between the two eigenvectors.

10. Summary and Discussion

We find that the dynamic heights of both reanalyses give mixed results when compared locally with in situ sea level data at tide stations. Pointwise comparisons between tide gauge sea levels and the reanalyzed dynamic heights at nearby grid

points show significant discrepancies, although some of their large-scale patterns are similar (Figures 3 and 4). The variance distributions in Figures 2 and 3 corroborate an underestimation of eastern boundary variability seen in the Table 1 statistics and show that the discrepancy is most severe in the annual component and north of the equator. The latter aspect is further reinforced by differences seen in the amplitude and phase of the annual component (Figure 4).

The distribution of available XBT data for assimilation is not a likely explanation for the underestimation. However, the wind information and the OGCM grid scheme are probably unable to adequately resolve the forcing and its oceanic response in the narrow coastal regions where the relevant oceanic scale is the coastal deformation radius (typically only a few tens of kilometers). Most ship reports come from farther offshore, the grid resolution is coarse for both wind fields, and orographic effects are not well resolved. Even if the wind forcings were accurate, the 1.5° zonal grid spacing of the ocean model does not resolve coastal currents within the coastal deformation radius (with their sharp offshore sea surface slopes). Although the amplitudes of the eastern boundary response are too small (Figures 2 and 3), the correlations for the nonseasonal variability are high (Figure 5) and fall off poleward. This seems most consistent with the low coastal resolution of the OGCM.

The comparisons improve over the ocean interior, west of 160°W, where data are available and the grid resolution for winds is not a factor. This analysis does not, however, assess the interior variability east of 160°W where tide gauges are lacking. The problems along the eastern boundary, per se, are probably of no concern to the climate prediction task. An important question that remains, however, is whether the coastal discrepancies affect the interior region offshore through Rossby wave propagation at low frequencies or are confined to the boundary zone.

Both reanalyses are proficient at reproducing an SSH difference index of the NECC variability in the west-central Pacific, both in the annual and the interannual bands. The annual cycle of the NEC index shows a 1 month lag in the reanalyses with respect to tide gauges, and incoherent month-to-month variability obscures the interannual variations of the NEC (tide gauges). For the SEC index the reanalyses show somewhat smaller velocities in the boreal summer and more serious discrepancies in the interannual band.

The reanalyses are best at reproducing large-scale temporal and spatial patterns in the departures from climatology. In particular, they both reflect the typical propagating ENSO cycle in upper ocean thermal structure captured in EOF analyses of the in situ data (three episodes, EOF modes 1 and 2). Variations in the ENSO cycle from one episode to another (EOF mode 3) are also simulated but less perfectly. The RA3 reanalysis is clearly superior in reproducing the large-scale modal breakdown of the tide gauge array in both the space and time domains. We conclude that the improvement is due primarily to the anomalous component of the FSU wind fields (RA3) being more accurate than the wind departures generated by the medium-range forecast model (RA2). The wind fields used are the only significant modification between the two reanalyses, and the wind field differences are dynamically consistent with differences in the reanalyzed variability of the dynamic height fields.

We find it significant that the assimilation of basin-wide ocean thermal data in the reanalyses does not override the deleterious effects of problems in the wind fields and that the resulting reanalyses can still vary significantly under variations in the wind variability. This suggests that wind field errors will quickly degrade model performance in the prediction mode, where the constraints of assimilated data no longer offset biases in the model evolution. It is, of course, impossible to use data-based wind analyses in such a real-time prediction system and it is also impractical for model initialization. Hence the most obvious route to improved performance of the prediction system is to improve the atmospheric MRF model. The results of this study also indicate that future atmospheric model modifications can be effectively evaluated by assessing them in reanalyses (such as RA2/MRF) against the best available standard (e.g., RA3/FSU) and/or against independent data sets (such as the tide gauge array). A more rigorous approach is to generate simulated forecasts for the same historical period in which data assimilation is suppressed after initialization.

Acknowledgments. This research has been supported under a research grant from the Eastern Pacific Climate Studies (EPOCS) program of the NOAA Environmental Research Laboratories. We thank the University of Hawaii Sea Level Center (G. Mitchum) and the Permanent Service for Mean Sea Level (D. Woodworth) for their assistance in compiling the monthly sea level data for tide gauges. We thank the NOAA National Meteorological Center (V. Kousky) for providing the sea level atmospheric pressure data. We are much indebted to M. Ji, D. Behringer, and T. Smith (all at NMC) for providing the reanalysis data and for helping us understand how the NMC analysis and forecast systems function.

References

Bryan, K., A numerical method for the study of the World Ocean, *J. Comput. Phys., 4*, 347-376, 1969.

Cox, M.D., A primitive, 3-dimensional model of the ocean, *Ocean Group Tech. Rep.* No. *1*, Geophys. Fluid Dyn. Lab., 143 pp., Princeton, N.J., 1984

Derber, J., and A. Rosati, A global oceanic data assimilation system, *J. Phys. Oceanogr., 19*, 1333-1347, 1989.

Harrison, D.E., On climatological mean wind stress and wind stress curl fields over the world ocean, *J. Climate, 2*, 57-70, 1989.

Hellerman, S., and M. Rosenstein, Normal monthly wind stress over the World Ocean with error estimates, *J. Phys. Oceanogr., 13*, 1093-1104, 1983.

Ji, M., A. Kumar, and A. Leetma, A multiseason climate forecast system at the National Meteorological Center, *B.ull Am. Met.eorol Soc., 75*, 569-577, 1994.

Ji, M., A. Leetma, and J. Derber, An ocean analysis system for climate studies, *Mon. Weather Rev. , 123*, 460-481, 1995

Levitus, S., Climatological atlas of the world ocean. *NOAA Prof. Pap. 13*,, 173 pp. U.S. Govt. Print. Office, Whasington, D.C., 1982

Mooers, C.N.K., A technique for the cross spectrum analysis of complex-valued time series, with emphasis on properties of polarized components and rotational invariants, *Deep Sea Res., 20*, 1129-1141, 1973.

Philander, S.G.H., and R. Pacanowski, The oceanic response to cross-equatorial winds (with application to coastal upwelling in low latitudes), *Tellus, 33*, 201-210, 1981.

Philander, S.G.H., W.J. Hurlin, and A.D. Siegel, A model of the seasonal cycle in the tropical Pacific Ocean, *J. Phys. Oceanogr., 17*, 1986-2002, 1987.

Reynolds, R.W., A real-time global sea surface temperature analysis, *J. Clim. 1*, 75-86, 1988.

Reynolds, R.W., and T. Smith, Improved global sea surface temperature analysis using optimum interpolation, *J. Clim., 7*, 929-948, 1994.

Sciremammano, F., A suggestion for the presentation of correlations and their significance levels, *J. Phys. Oceanogr., 9*, 1273-1276, 1979.

Wyrtki, K., Sea level and the seasonal fluctuations of the equatorial currents in the western Pacific Ocean, *J. Phys. Oceanogr., 4*, 91-103, 1974a.

Wyrtki, K., Equatorial currents in the Pacific 1950 to 1970 and their relation to the Trade Winds, *J. Phys. Oceanogr., 4*, 372-380, 1974b.

D. B. Enfield and J. E. Harris, Atlantic Oceanographic and Meteorological Laboratory, NOAA, 4301 Rickenbacker Causeway, Miami, FL, 33149. (e-mail: enfield@ocean.aoml.erl.gov)

(Received August 4, 1994; revised January 24, 1995; accepted March 2, 1995.)